Improving Model-Based Visual Self-Localization Using Gaussian Spheres

D. Gonzalez-Aguirre, T. Asfour, E. Bayro-Corrochano and R. Dillmann

Abstract A new approach for global self-localization based on a world model and active vision using varying density gaussian spheres is introduced. The method simultaneously improves and extends our previous proposed approach [1] by contemplating the acquired uncertainty in the perception layer. The used appearance-based object recognition components deliver noisy percept subgraphs which are filtered and fused into an ego-centered frame. In subsequent stages, the required vision-to-model associations are extracted by selecting ego-percept subsets in order to prune and match the corresponding world-model-graph. Ideally, these coupled subgraphs hold necessary information to obtain the model-to-world transformation, i.e. the pose of the robot. However, the estimation of such a pose is not robust due to the uncertainties introduced while recovering euclidean metric from images and the mapping from the camera to the ego-center. In this context, our approach models the uncertainty of the percepts with a radial normal distribution. This setup allows an optimization-solution in a closed-form, which not only obtains the maximal density position depicting the optimal ego-center, but it also ensures a solution even in situations where normal spheres might not meet at all.

1 Model-Based Visual Self-Localization

The following resume of our previous approach offers a brief overview of the elements and their mechanisms involved in the vision-based self-localization, in this way a better understanding of the improvements and extensions in the following

D. Gonzalez-Aguirre, T. Asfour, R. Dillmann
Institute of Computer Science and Engineering, University of Karlsruhe, Haid-und-Neu-Strasse 7, Karlsruhe-Germany, e-mail: {gonzalez,asfour,dillmann}@ira.uka.de

E. Bayro-Corrochano
CINVESTAV, Av. Cientifica 1145, Zapopan-Jalisco, Mexico, e-mail: edb@gdl.cinvestav.mx

content is possible. However, it is strongly suggested to see all the details of our previous publication [1] available at *http://i61www.ira.uka.de/users/gonzalez/*.

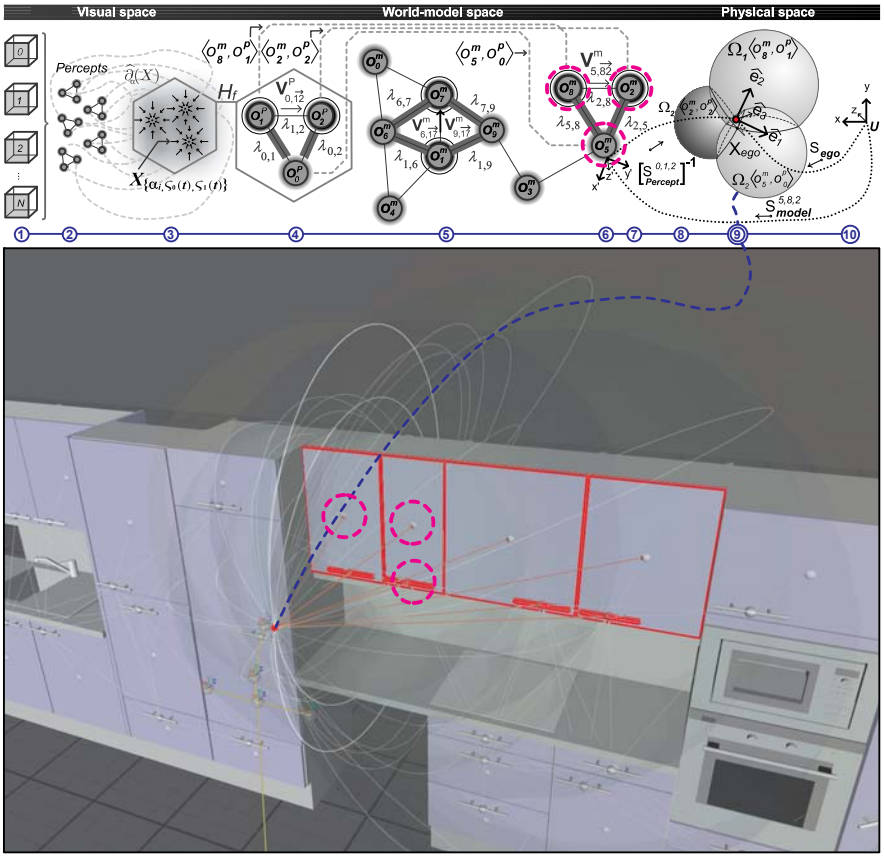

Fig. 1 The Model-Based Visual Self-Localization approach. 1) Appearance-based object recognition components. 2) Extracted percepts mapped into the ego-frame. 3) Multi-trial percepts fusion. 4) Fused ego-percepts with their corresponding world-model associations. 5) Proximity filtering for pruning purposes upon world-model. 6) Orientation filtering. 8) Hypotheses generation-validation. 9) Geometric and statistical optimization. 10) Pose estimation.

Fig.1 shows the three spaces concerning the self-localization. The visual space refers to the stratum of the process where the image information from the world is stored. The world-model space is the graph-based ontologie of the world, here there are two sublayers, the geometric (with the 3D vertices and their composition information) and the topological layer, describing the interrelation of object components layers. Finally the physical space where the robot is located has to be revealed by means of the following phases.

The appearance-based object recognition components receive raw images and deliver the type and position of the recognized elements within visual space. The

management of this visual-spatial scanning is planned based on the geodesic ego-sphere and the 3D field of view resulting from the stereo calibration, see Fig.3.

The extracted percepts are mapped into a static common ego-frame, in this manner multiple perception-instance of the same object are fused to define a robust percept. Once there is an ego-image, i.e. a fused-filtered set of percept, then the matching which associates the vision-percepts with the world-model takes place by means of two filtering stages.

The fast proximity filtering reduces the searching space by simultaneously exploiting the precomputed distance table and partitions of the graph. The remaining candidates are matched against a more elaborated filtering criterion, which is based on the relative orientation among those remaining nodes. The latter computations model the implicit effects of noise and other uncertainties. It is important to remark that these phases are parametrically tuned to reject those model subgraph-components or nodes which clearly diverge from the ego-image because in the following stage the remaining outliers will be robust and easily removed.

At this point there are few matched subgraphs from one side in the world-model on the other side the ego-image. This would actually mean that the robot may be in many locations at the same time. These location hypotheses need to be generated and disambiguated by means of geometric and topological constrains implicit within the same ego-image.

The proposed solution implies the main idea of the approach, i.e. the measurement of each percept provides only information about the proximity between the robot and the object in question, this defines a restriction subspace (sphere) where the ego-center most be located in reference to the matched model object. This concept is further exploited by using more from these subspaces which have to be composed in a constrained geometric structure to hold the world-model composition and percepts space instances. The latter ideas turn out to be a composition of noisy spheres which by means of the following method could be modeled and solved.

The following sections describe the sources and nature of the uncertainties, which are modeled and optimized by following proposed technique to find the maximal density position.

2 Uncertainty

The critical role that the uncertainty plays in our previous approach cannot only strongly diminish the precision of the estimated pose, but it can also menace the existence of it by drawing away the intersection of the restriction subspaces, i.e. the spheres might not intersect because of accumulated errors introduced in the perception layer.

In order to sagaciously manage this condition and other derived side effects, it is crucial to reflect upon the nature of the acquired uncertainties in connection with our localization approach. In this context, there are two remarkable sources of uncertainty, the *image-to-space* and the *space-to-ego* uncertainties.

2.1 Image to Space Uncertainty

The image-to-space uncertainty obtained from the appearance based vision recognition process (see [1], section 2.1) starting with the pixel precision limitations (e.g. noise, discretization, quantization, etc.) and ending with the errors-limitations of the camera model and its calibration (e.g. radial-tangential distortion and intrinsic parameters [2]) could be modeled (according the central limit theorem[5]) as a normal distribution where the variance is strongly related to the perceptions depth

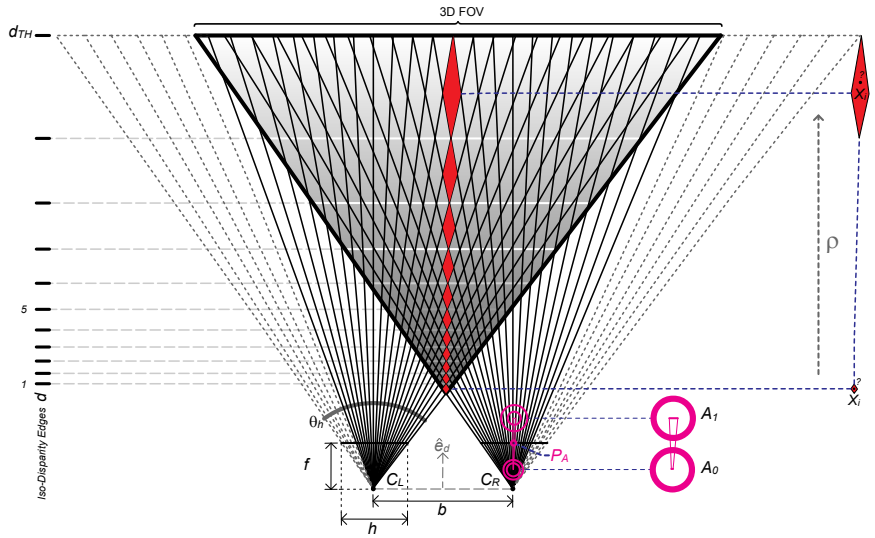

Fig. 2 The image-space uncertainty factors in a front-parallel configuration.

$$\rho_i = (x_i - C_L) \cdot \hat{e}_d, \tag{1}$$

i.e. distance between camera center C_L and point in space x_i along the stereo rig normal vector $\hat{e}_d$, see Fig.2,

$$\sigma_i \cong \frac{1}{\zeta}\rho_i^2, \tag{2}$$

where $\zeta > 1 \in \Re$ is an empirical scalar factor depending on the resolution of the images and the vergence angle of the stereo rig.

This variance model arises from the following superposed facts: first, considering only the monocular influence in each camera of the stereo rig, there the surface patch A_i on the plane perpendicular to the optical axis of the camera (see Fig.2) imaged into a single pixel P_A grows linearly as function of the distance ρ_i

$$A_i = 4\rho_i \tan\left(\frac{\theta_h}{2h}\right)\tan\left(\frac{\theta_v}{2v}\right), \tag{3}$$

where θ_h and θ_v represent the horizontal and vertical angular apertures of the field of view, whereas h and v depict the corresponding resolution of the image. Consequently, the stereo triangulation has an additional effect, i.e. during the estimation of the 3D position $\mathbf{M}_{stereo}(X_i)$ of a matched pair of points on left x_i^L and right x_i^R images the distance ρ_i affects the magnitude of the disparity d_i, therefore the precision of the computations, i.e. the points which are closer to the base line have wider disparities along the epipolar lines, meanwhile those points located after distance $\rho_{Th} > fb$ have a very narrow disparity (falling in subpixel domain $d < 1$) which results in inaccurate depth calculations. This situation also produces a sparse distribution of the iso-disparity [3] surfaces, meaning that the subspace contained between this surface-strata grows as

$$d_i = \frac{fb}{\rho_i}, \tag{4}$$

where the focal f distance and the base line size $b = ||C_L - C_R||$ play relevant roles in the measurement precision.

Fig.2 shows the iso-disparity edges delineating the subspaces contained between two discreet steps (pixel increment) in the disparity relation of Eq.4. In this manner, points contained within one of these subspaces will produce same discreet disparity when matching the corresponding containing pixels. Hence, the uncertainty ought to be proportional to the distance contained among iso-disparity edges. These two factors applied produce an uncertainty which grows in an amortiguated quadratic pattern which we reflect in our model as a variance spreading in the same fashion.

2.2 Space to Ego Uncertainty

The space-to-ego uncertainty acquired while relating the pose of the percepts from left camera frame to the ego-frame (head base frame of the humanoid robot, see Fig.3-a) is produced due to the physical and electronic measurement inaccuracies, which are substantially magnified by projective effects, i.e. the almost negligible errors in the encoders and mechanical joints of the active head of the humanoid robot are amplified proportional to the distance ρ_i between the ego center and the location of the percept.

Fig.3-b shows the kinematic chain starting at x_i^L, which are the left camera coordinates of the space point X_i. Subsequently, the transformation from the left camera frame C_L to the shoulders base $T(t)$, passing through the eyes base H and neck frame $N(t)$, is given by

$$\acute{X}_i = \mathbf{M}_{ego}^t(x_i), \tag{5}$$

$$\mathbf{M}_{ego}^t = [T_{(t)}N_{(t)}HC_L]^{-1}, \tag{6}$$

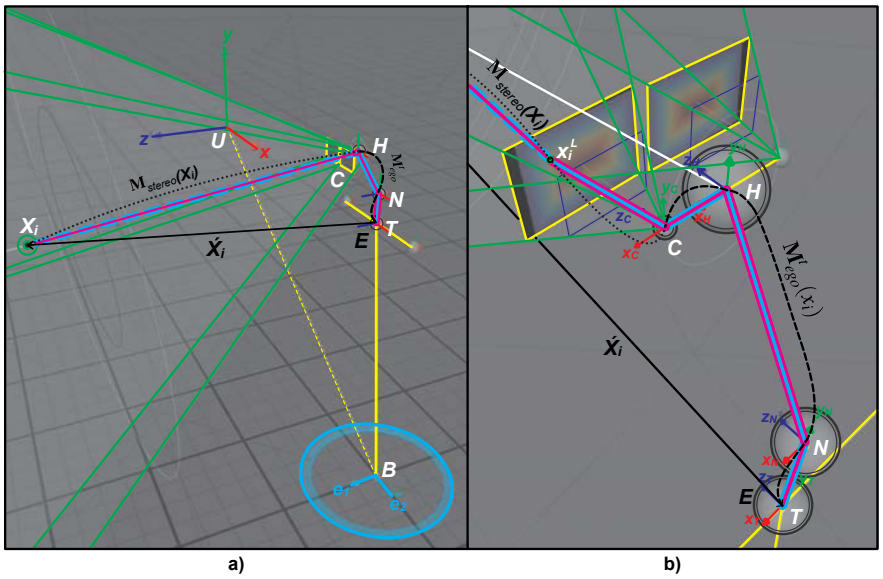

Fig. 3 The space-ego uncertainty acquisition process produced by the mapping percepts from camera coordinates to the ego-frame. a) The whole transformation $\acute{X}_i = \mathbf{M}^t_{ego}(\mathbf{M}_{stereo}(X_i))$. b) The transformation $\mathbf{M}^t_{ego} = [T_{(t)}N_{(t)}HC_L]^{-1}$.

where $\mathbf{M}^t_{ego}$ is the ego-mapping at time t. Here, the transformations $T_{(t)}$ and $N_{(t)}$ are time depending because they are active during the scanning strategy.

3 Geometry and Uncertainty Model

Once the visual recognition components have delivered all classified percepts within a discreet step in the scanning trajectory (a trial), these percepts are mapped into a reference ego-frame using Eq.5 of the kinematic chain of the robot. This ego-frame E is fixed during the scanning phase, in this fashion all percepts from different trials are located in a static common frame, see Fig.3-b.

The unification-blending process done by the fusion phase (see [1], section 2.1.1) simultaneously allows the rejection of those percepts which are far from being properly clustered and creates the delineation set which is later melted into a fused percept.

At this point percepts are matched against the model identities based on the techniques exposed in [1]. Next, the geometric and statistical phase which determines the position of the robot base on intersection of spheres is properly formulated by introducing the following gaussian sphere and its apparatus for intersection-optimization.

3.1 Gaussian Spheres

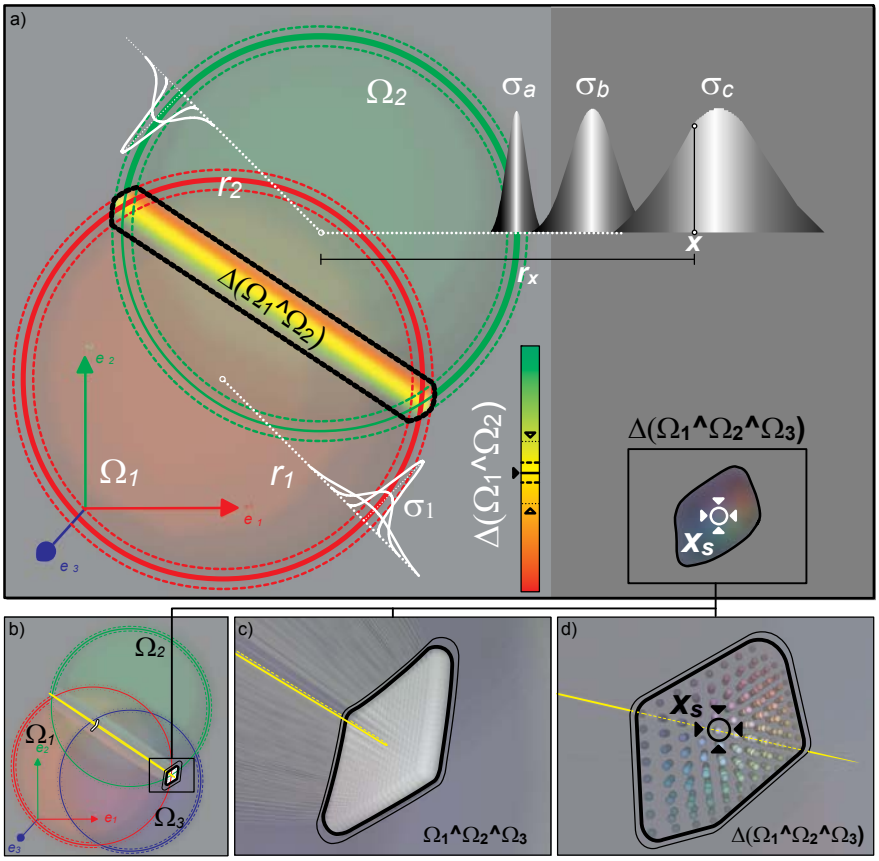

Fig. 4 The Gaussian Spheres meeting. a) Two gaussian spheres meeting $\Omega_1 \wedge \Omega_2$ describing a density subspace $\Delta(\Omega_1 \wedge \Omega_2)$. b) Three gaussian spheres $\Omega_{i=1,2,3}$ meeting in two regions depicting a subspace $\Omega_1 \wedge \Omega_2 \wedge \Omega_3$. c) Detail view of one of the previous subspaces. d) Discreet approximation of the maximal density location x_s. e) Detail of the implicit density space $\Delta(\Omega_1 \wedge \Omega_2 \wedge \Omega_3)$. f) Implicit radius r_x when estimating the density at position x.

The considered restriction spheres Ω_i (see [1], section 2.4) are endowed with a soft density function

$$\widehat{f}(\Omega_i, x) \mid x \in \Re^3 \mapsto (0,1] \in \Re, \tag{7}$$

the density value decreases exponentially as a function of the distance from an arbitrary point x to the surface of the sphere Ω_i

$$S(x, X_i, r_i) = ||x - X_i|| - r_i, \tag{8}$$

$$\widehat{f}(\Omega_i, x) = e^{\frac{-S(x,X_i,r_i)^2}{2\sigma_i^2}}, \tag{9}$$

this function depicts the non-normalized [1] radial normal distribution

$$\check{N}(\mu := \{x \mid \ker(S(x, X_i, r_i))\}, \sigma_i^2) \tag{10}$$

for x to be in the surface of Ω_i, i.e. the null space of $S(x, X_i, r_i)$.

Now, the density of a point x in relation with a sphere Ω_i represents the non-normalized probability for the point to belong to the surface of the sphere. As a desired consequence the maximal density will be on the surface of the sphere itself. In order to apply the same essential idea used to find the robot position using intersection of restriction spheres it is necessary to propose a mechanism to effectively deal with these concepts.

In the following sections the restriction spheres and their conjuncted composition properly model both uncertainties, allowing the meeting of spheres by finding the subspace where the maximal density is located, see Fig.4.

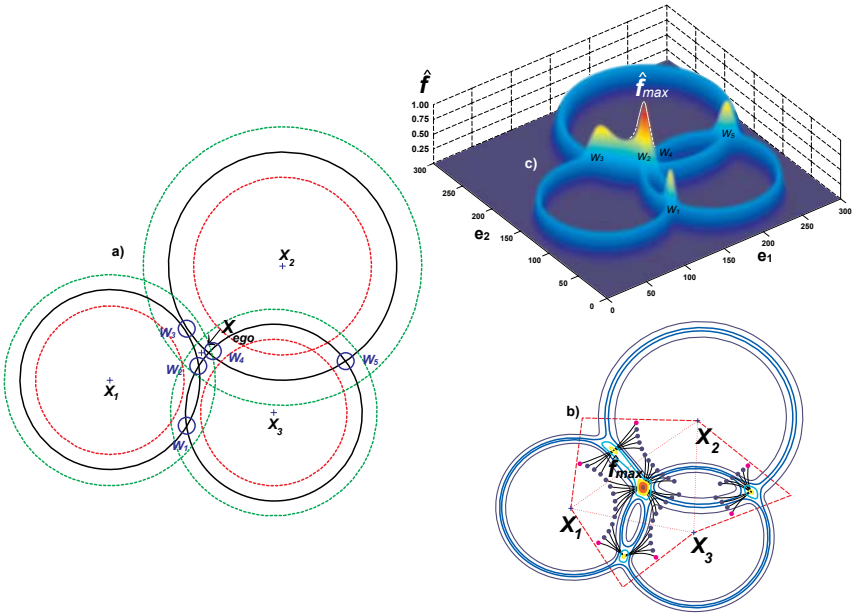

Fig. 5 The Gaussian Circles, i.e. 2D Gaussian Spheres. a) Three gaussian circles setup. b) The total accumulative density $\widehat{f}_c(x) = \sum_i^n \widehat{f}(\Omega_i, x)$ allows a better visualization of the composition of its product counterpart $\widehat{f}_t(x)$, see also 6. c) Density contours with seeds and their convergence by means of gradient ascendant methods.

[1] By the factor $\frac{1}{\sigma\sqrt{2\pi}}$, because the proposed function models only the density.

This could be understood as an isotropic dilatation or contraction of each sphere in order to meet at maximal density of the total density function $\widehat{f}_t(x) \longrightarrow (0,1] \in \Re$

$$\widehat{f}_t(x) = \prod_i^n \widehat{f}(\Omega_i, x). \tag{11}$$

Due to the geometric structure composed by n spheres it is possible to foreseen the amount of peaks and the space regions $\mathbf{W}_s$ where the density peaks are located. Therefore, it is feasible to use state of art gradient ascendant methods [4] to converge to the modes using multiple seed strategically located based on the spheres centers and intersection zones, see Fig.5-c. Finally, the seed with maximal density represents the solution position x_s

$$x_s = argmax_{x \in K}\ \widehat{f}_t(x), \tag{12}$$

however, there are many issues of this shortcoming solution. The iterative solution has a limited precision by the parameter used to stop the shifting of the seeds. In addition, the location and spreading of the seeds could have a tendency to produce undesired phenomena as oscillation, under or oversampling (bandwidth-kernel selection issue) and all other disadvantages that iterative methods present.

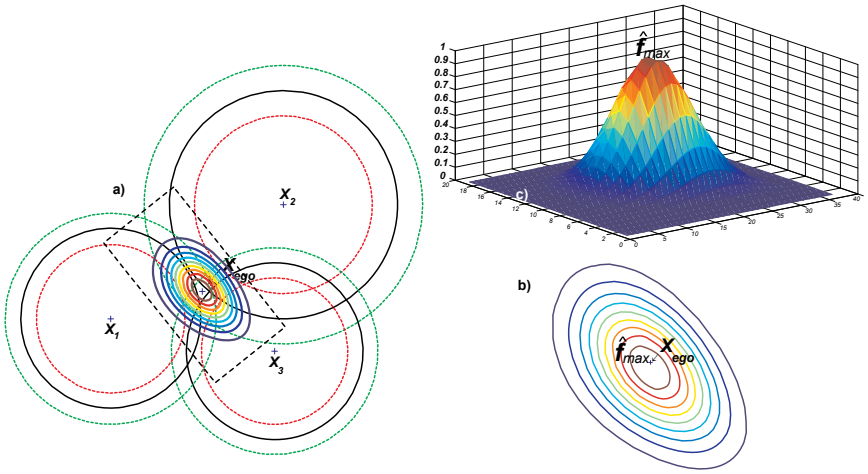

Fig. 6 The Gaussian Circles, i.e. 2D Gaussian Spheres. a) Three gaussian circles setup. b) The total density $\widehat{f}_t(x) = \prod_i^n \widehat{f}(\Omega_i, x)$. c) Density contours and ego-center X_{ego}, notice that the resulting distribution is not gaussian.

The optimization assignment expressed by Eq.12 could be properly solved in a convenient closed-form. In order to address the solution x_s it is necessary to observe the configuration within a more propitious space, which simultaneously allows an advantageous representation of the geometrical constrains and enables an efficient

management of the density, i.e. incorporating the measurements according their uncertainty and relevancy while avoiding density decay.

3.2 Radial Space

The key to attain a suitable representation of the latter optimization resides in the exponent of the Eq.9. There, the directed distance from a point x to the closest one on the surface of the sphere is expressed by the Eq.8. Even more, when considering the total density function (see Eq.11) it unfolds the complexity by expressing the total density as a tensor product.

The inherent nature of the problem lies in the radial domain, i.e. the expression $S(x,X_i,r_i)^2$ is actually the square magnitude of the difference between the radius r_i and the implicit defined radius r_x between the center of the spheres X_i and the point in question x, see Fig.4-f. Hence, the optimization configuration cannot only be better expressed in radial terms, but also the geometrical constraints restricting the relative positions of the spheres could be naturally uncluttered as follows.

3.3 Restriction Lines

Consider the case of two spheres Ω_1 and Ω_2, see Fig.7-a. Here, their radii and the distance between their centers $\delta_{\overline{1,2}} = ||X_1 - X_2||$ allow the formulation of the following geometric restrictions, which ensure the intersection of the spheres in at least a single point P_χ. This restriction is expressed as the inequation line L_χ, which describes the radial configuration subspace represented by pairs of the form $P_\chi = [r_1, r_2]^T$, the intersection of spheres $\Omega_1 \wedge \Omega_2$.

Notice that the inequality line divides the configuration space into two regions, the half space partially holding the restriction imposed by the inequation line L_χ, however it still has configurations which produce empty intersection of spheres, e.g. any configuration holding $r_2 \geq \delta_{\overline{1,2}} + r_1$. In order to prevent these degenerated configurations there are two additional restriction inequation lines, which could be unveiled by following a similar pattern.

In the same fashion, Fig.7-b shows the case where the minimal contact point P_β occurs, subject to $r_1 \geq \delta_{\overline{1,2}} + r_2$. In this configuration the sphere Ω_1 fully contains the sphere Ω_2 and their surfaces intersect solely at P_β. Once again, in order to ensure at least this contact point, the fluctuation of the radii of both spheres is restricted by a linear relation comprehensibly expressed by the inequality line L_β. The latter restriction actually happens in a symmetric manner (by interchanging the roles from Ω_1 with Ω_2) resulting in a third restriction, i.e. the inequality line L_α, see Fig.7-c,d.

As a result, the configuration space is delineated into four regions K_α, K_β, K_χ and K_{meet} all open except K_χ. Only those configurations within the subspace K_{meet} represent non-empty intersections of the spheres, e.g. the point $x_{conf} = [r_1^{'}, r_2^{'}]^T \in$

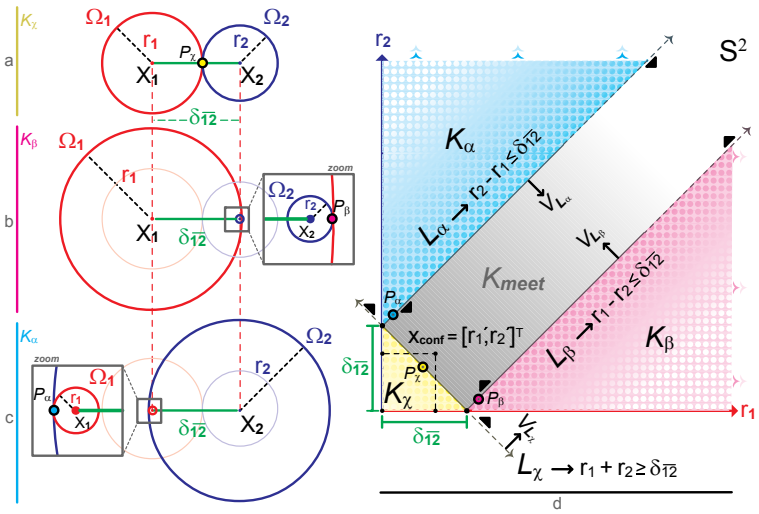

Fig. 7 The intersection of spheres restriction lines derivation in the radial space $\mathbf{S}^2$. a) The line L_χ implicates the first restriction for ensuring non empty intersection of spheres. b) The derivation of reminding right side empty intersection restriction line L_β. c) The left side symmetric case, generating the third restriction line L_α.

K_{meet} , see Fig.7-d. This representation implicates that those points on the edge of K_{meet} depict intersections of spheres in a single point (circle with null radius), whereas elements within K_{meet} represent intersection depicting a circle with non zero radius.

Latter representation soundly amalgamates the distance among centers of the spheres with their radii producing a robust and general criteria to establish intersection guarantee, see Fig.7-d.

3.4 Restriction Hyperplanes

The previous derivation of the restriction lines was achieved by considering only the case involving two spheres, however, it is possible to extend these restrictions to n spheres.

Formally, this affirmation is theoretically supported by representing the n spheres radial configuration space $\mathbf{S}^n$ as the *Hilbert* space $\mathbf{C}^n$, where each dimension depicts the radius of one sphere, i.e. an element $x_{conf} \in \mathbf{S}^n$ of the n-dimensional radial configuration space can be uniquely specified by its coordinates with respect to an orthonormal basis vectors $\hat{e}_i \in \mathbf{S}^n \mid i \in \{1, \cdots, n\} \subset \mathbf{Z}$ are perpendicular to each other because the radius of each sphere is independent from the rest. In this manner, the previous restriction lines could be perpendicularly extruded in $n-2$ dimensions creating the restriction hyperplanes $\Phi_\alpha^{(i,j)}$. Here again, each hyperplane divides the

space in two subspaces, i.e. configurations within the region opposite to the normal vector V_{L_α} represent non intersecting spheres, see Fig.8.

Even more, the set of hyperplanes expressed in their hessian could be used to compose a matrix inequality

$$\mathbf{A}x \leq b, \tag{13}$$

where $\mathbf{A}$ is a $m \times n$ matrix, with m bounding half-spaces (normal vectors of the hyperplanes) and b represents a $m \times 1$ column vector formed by stacking the Hessen distances of the hyperplanes, i.e. an open polytope, see Fig. 8.

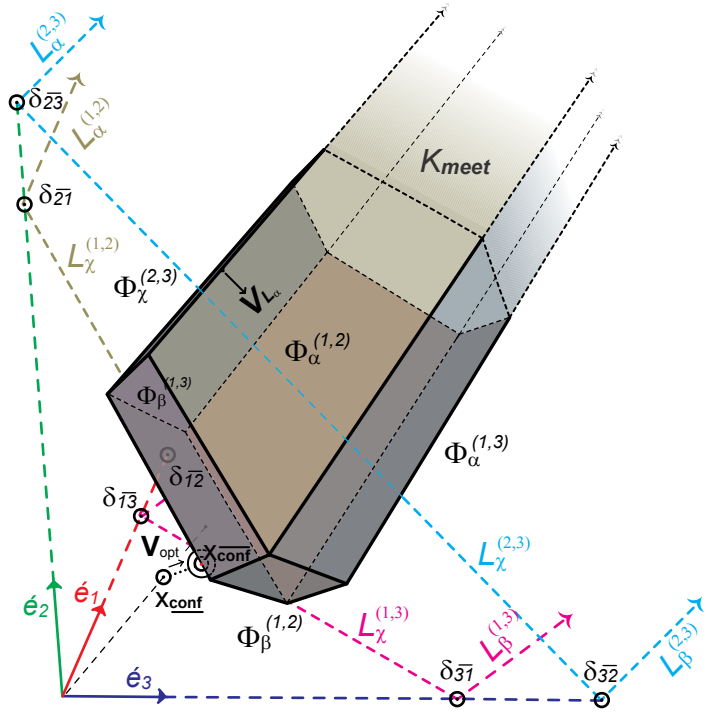

Fig. 8 The radial density space $\mathbf{Sb}^3$ containing the open polytope which delineates the subspace K_{meet}. Observe the transformation-optimization vector V_{opt} which implies an isotropic variation in the underlying density domain while creating a general dilatation within the implicit radial domain.

Consider the case where $n = 3$, three spheres implying an open polyhedron, within this radial space each line $L_\alpha^{(i,j)}$, $L_\beta^{(i,j)}$ and $L_\chi^{(i,j)}$ is extruded in the complementary dimension creating restriction planes given by $\Phi_\alpha^{(i,j)}$. Next, the face cells, ridges and vertices of the polytope are found using our rather simple but fast implementation for *vertex enumeration*[6], see Fig.8.

At this stage, it could be conveniently established whether the current configuration is a valid or not, in other words, determine if the point x_{conf} belongs to the polytope. This assertion is formally given by $\mathbf{A}x_{conf} \leq b$. In case this assertion is held, then there is no need to go through the following optimization phase because the spheres are meeting on their solid surface. Thus, it results into a maximal density, i.e. $\widehat{f}(\overline{x_{conf}}) = 1$.

The opposite situations represent those degenerated configurations resulting from noise measurements and previously discussed errors, e.g. the point $x_{\underline{conf}}$ represents an invalid configuration, out side of the polytope, see Fig.8.

The target solution for the latter cases necessarily implies a decay in the density, because at least one of the vector components has to be modify for the point $x_{\underline{conf}}$ in order to become a valid configuration $x_{\overline{conf}}$. This offset signifies a dilatation (or relative contraction) of the sphere(s) depending on the direction of the displacement

$$x_{\overline{conf}} = x_{\underline{conf}} + V_{opt}, \tag{14}$$

which transforms the degenerated configuration into a valid one, see Fig.8.

Here, the optimal criterion to calculate the transformation V_{opt} is to accomplish the minimal length offset vector $V_{opt} := [v_{r_1}, ..., v_{r_n}]$, i.e. retaining as much density as possible by eluding degradation of the spheres (reducing the needed radial variance) $S(x_{\underline{conf}} + V_{opt}, X_i, r_i)$ on Eq.9.

The geometric intuitive way of finding such a vector is by seeking the closest point from $x_{\underline{conf}}$ on the cells or ridges of the polytope, which could be efficiently computed by perpendicularly projecting the point $x_{\underline{conf}}$ to each hyperplane

$$x_{\overline{conf}}^{(i,j)} = x_{\underline{conf}} - (V_{\alpha}^{(i,j)} \cdot x_{\underline{conf}}) V_{\alpha}^{(i,j)}, \tag{15}$$

and selecting the closest one from those holding the assertion given by Eq.13.

Although this technique is computational efficient and geometric effective the outcoming solution is no the optimal one, because within this space only the absolute directed distance is considered, no contribution effects of different variances are assessed, which does not necessarily mean the minimal density decay.

This limitation could be defeated by considering a *homothety* transformation $\mathbf{H}(\mathbf{S}^n)$ (a variance normalization) of the radial configuration space inspired on the essential concept of the *Mahalanobis* distance[5] as follows.

The spatial density function of a gaussian sphere Ω_i given by Eq.9 could be conveniently reformulated in the radial domain as

$$\widehat{f}(\Omega_i, x) = e^{-\frac{1}{2}\left(\frac{r_x}{\sigma_i} - \frac{r_i}{\sigma_i}\right)^2}, \tag{16}$$

in such a way the variance of the endowed normal distribution scales the implicit defined radius r_x and the mean radius r_i of the sphere Ω_i by a $\frac{1}{\sigma_i}$ factor. This normalization mapping could be generalized for the whole radial configuration space $\mathbf{S}^n$ as

$$\mathbf{H} = diag\left[\sigma_1^{-1}, \sigma_2^{-1}, \ldots, \sigma_n^{-1}\right]. \tag{17}$$

This matrix actually represents the inverse covariance matrix Σ^{-1} of the total density function given by Eq.18. This could be easily visualized by the alternative expression[2]

$$\widehat{f_t}(x) = e^{-\frac{1}{2}\sum_{i=1}^{n}\left(\frac{||x-X_i||}{\sigma_i}-\frac{r_i}{\sigma_i}\right)^2}. \tag{18}$$

Based on this expression and taking into account the uncorrelated radial distributions, it is clear that the underlying covariance matrix $\mathbf{H}^{-1} = \Sigma$ has null elements outside its trace. In this fashion, the proposed normalization $\mathbf{Sd}^n = \mathbf{H}(\mathbf{S}^n)$ could take place by applying the matrix $\mathbf{H}$ as an operator over the orthonormal vector bases of $\mathbf{S}^n$ as

$$\acute{e}_i = H\hat{e}_i. \tag{19}$$

The euclidean metric within this resulting space is uniformly isomorphic with the density space, i.e. displacements of the same length arising from the same position imply equal density decay in all directions. In our implementation this normalization takes place before the polytope has been computed, reflecting the effects within the affine[3] strata while computing the optimal points in Eq.15, see Fig.8.

The application of the previous methods within the normalized radial configuration space $\mathbf{Sd}^n$ ensures not only the optimal solution (minimal decay), but it also vantages from the available certainty provided from those spheres with smaller variance (higher reliable percepts) by introducing smaller displacements in the corresponding dimension of the displacement vector $V_{opt} \in \mathbf{Sd}^n$.

In other words, the spheres which have a wider variance can easily expand or contract their surfaces than those with smaller ones, in order to obtain the highest possible density at the meeting operation. The method delivers the optimal tradeoff-fusion while performing the management of the modeled uncertainty.

3.5 Duality and Uniqueness

In case the latter method has taken place in $\mathbf{Sd}^3$ (by considering three spheres) obtaining the optimal configuration $x_{\overline{conf}} \in \mathbf{Sd}^3$, there is still a duality to solve while back mapping this configuration into the physical euclidean space. This issue is solved straightforward by computing the pair of points solution

$$J_{\wedge_{i=1}^{3}} = \bigwedge_{i=1}^{3} \Omega_i(\sigma_i(x_{\overline{conf}} \cdot \hat{e}_i), X_i), \tag{20}$$

and verifying against the valid subspace for each of the hypotheses positions, i.e. ratifying which of the points is inside the room. In case the both solutions lie within

[2] By rewriting the exponent as a vector column and arranging in a standard form $x^t \Sigma^{-1} x$.

[3] In the Hessen normal form of the hyperplanes.

the valid subspace the simple cross match against the location of other percepts will robustly disambiguate the solution.

It is possible to obtain an unique solution by using four spheres for the optimization task, i.e. to represent the setup within $\mathbf{Sd}^4$. In this way $x_{\overline{conf}} \in \mathbf{Sd}^4$ could be again mapped back into the physical euclidean space by means of meet operator as

$$P_{\bigwedge_{i=1}^{4}} = \bigwedge_{i=1}^{4} \Omega_i(\sigma_i(x_{\overline{conf}} \cdot \hat{e}_i), X_i), \tag{21}$$

unveiling the position of the robot. In our approach the vertex enumeration in higher dimensions ($n > 3$) is still under development, thus experimental results are optimized in $\mathbf{Sd}^3$.

4 Conclusion

This approach extends and improves our previous methods to solve the model-based self visual localization using conformal geometric algebra and gaussian spheres. The proposed method translates the statistical optimization problem of finding the maximal density location for the robot into a radial density space which allows a very convenient description of the problem. Within this domain it is possible not only to draw the geometric restrictions which ensure the intersection of spheres, but it also enable us to find the optimal fusion and tradeoff of the available information provided by the precepts by regarding the provided information of each landmark according its uncertainty.

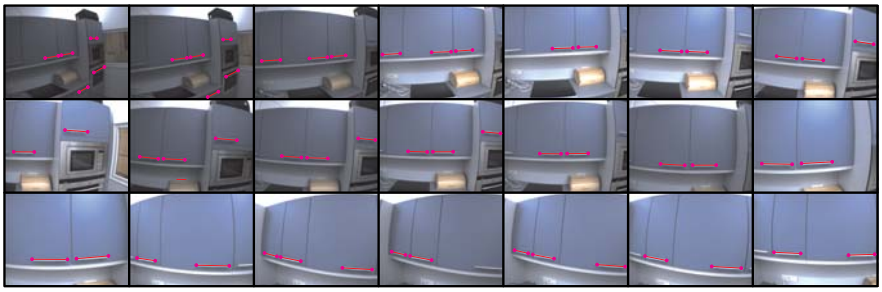

Fig. 9 The scanning sequence executing the self-localization, the results from the handler recognition component are highlited.

We have also discussed and modeled the uncertainty sources including all phenomena from the image processing up to encoder in the robotic joints. The timing of the whole approach could be seen in previous approach with the exception to the vertex enumeration which take approximately $15-50$ ms depending on the configura-

tion. The overall precision available at the moment[4] is ± 2.75 cm by comparing with the measurement of the distance between the ego center and the origin of the universal coordinate system, see Fig.9. However, the experimental results are not complete because the vertex enumeration under development will allow us to compare the effects of involving more than three the orientation. The upcoming extensive result and videos will be made available at *http://i61www.ira.uka.de/users/gonzalez/*.

There are still open question about the performance, quality and timing of using more spheres and subpixel precision methods like lines instead of single pairs of matched points. In particular the role of line segments in the class recognition will a deep impact. This features can be extracted robustly and will be tested.

References

Due to the character of this paper it is suggested to see all references included in the reference paper.

1. D. Gonzalez-Aguirre, T. Asfour, E. Bayro-Corrochano and R. Dillmann : Model-Based Visual Self-Localization using Geometry and Graphs. In: To Appear ICPR. Tampa, Florida (2008)
2. R. Hartley and A. Zisserman: Multiple View geometry in computer Vision. Cambridge University Press (2004). ISBN 0521540518.
3. M. Pollefeys, L. Van Goo, M. Vergauwen, F. Verbiest, K. Cornelis, J. Tops and R. Koch : Visual Modeling with a Hand-Held Camera. In: International Journal in Computer Vision. Hingham, MA, USA, 207–232 (2004)
4. T. Korn and A. Granino, Mathematical handbook for Scientists and Engineeres. Dover Publications, Dover UK. ISBN 0-486-41147-8.
5. O. Kallenberg : Fundations of Modern Probability. New York: Springer-Verlag, 1997.
6. D. Avis and K. Fukuda: A pivoting algorithm for convex hulls and vertex enumeration of arrangements and polyhedra. In: International Journal of Discrete Computational Geometry, 8:295-313, 1992.

[4] These are still the results of the non-optimized implementation.